




Optical Frequency Comb Generation via Cascaded Intensity and Phase Photonic Crystal Modulators

Henry Francis , Xiao-Dong Zhang, Si Chen, Jia-Wang Yu, Kai-Jun Che , *Member, IEEE*,
Mark Hopkinson, and Chao-Yuan Jin 

Abstract—Nanophotonics, driven by low processing power and high density integration, is appearing as the next logical step for microwave photonics. Optical frequency combs (OFCs), which play a vital role in integrated microwave photonics, have not yet generated using nano-structured devices. In this paper, we propose OFC generation based on all-optical modulation of nanophotonic structures. A theoretical model based on temporal coupled mode theory is developed to describe cascaded all-optical photonic crystal intensity and phase modulators. Using a modulation light with a sinusoidal waveform, a separate carrier light is modulated to generate an OFC. By manipulating the modulation power and device dimensions, a flat OFC that spans over a 600 GHz is delivered. The proposed system offers OFC generation with tunable comb line spacing using devices with high density integration capabilities.

Index Terms—Microwave photonics, nanophotonics, optical frequency comb, photonic crystal.

I. INTRODUCTION

THE convergence of integrated photonic technologies with microwave photonics (MWP) has led to increased on-chip device functionality [1]. In much the same way that MWP produced new functionalities by combining microwave and photonic engineering, integrated MWP produces unique device capabilities. With advanced fabrication techniques and the integration of microscale photonic devices, the enhanced nonlinear

interactions present in small-scale devices have enabled new technologies. These technologies include plasmonic modulators [2], on-chip stimulated Brillouin scattering [3] and on-chip optical frequency comb generators [4].

Continuing on this same trend, on-chip integration of nanophotonic devices is expected to increase optical nonlinearity, decrease device footprint and thus enhance the progressing research field of integrated MWP. Photonic crystal (PhC) devices are currently emerging as a contender for the implementation of nanophotonics. Strong light confinement in ultra-small mode volumes (V) and ultrahigh quality (Q) factors enables promising functionalities in on-chip all-optical processing [5], [6]. Indeed, cutting edge studies have shown small volume all-optical modulators [7], low power EO modulators [8] and low threshold topological lasers [9], all implemented using photonic crystal devices. To this end, implementing standard MWP components using a photonic crystal platform would open the area of MWP further. One such component that is yet to be realised in nanophotonics is an optical frequency comb (OFC) generator.

Among the available OFC generation technologies, optical parametric oscillation based on micro-resonators has hitherto prevailed as a simple and elegant solution towards on-chip OFCs [4]. With careful consideration of the dispersion characteristics, optical nonlinearity and fine tuning of the pump laser, chip-scale coherent OFC generators have been realised [10]. However, the pump to comb efficiency can be very low, often less than 1% for the bright soliton case [11]. Furthermore, micro-resonator based combs produce a fixed spacing between comb lines which is dependant on the resonator size. In this paper, a novel method to generate an OFC with a tunable mode spacing that has the potential for on-chip nanophotonic integration is proposed.

Another method of OFC generation which has been explored in detail is the use of electro-optic (EO) modulators [12]. Using EO modulators to generate an OFC increases the input power to OFC efficiency when compared to micro-resonator Kerr combs. Commercially available lithium niobate (LN) EO modulators can have a half wave voltage down to 2–3 V, which enables highly efficient OFC generators [13]. The mechanism used is the refractive index change via EO modulation based on the large LN EO coefficient. In order to scale down LN modulators, great progress has also been made towards integrated LN modulators based on thin-film LN [14], [15]. This work showed low half wave voltages, 3.5 V - 4.5 V, over a large bandwidth, 5-40 GHz.

Manuscript received June 1, 2020; revised October 20, 2020 and November 23, 2020; accepted November 24, 2020. Date of publication December 2, 2020; date of current version January 14, 2021. This work supported by the EPSRC First Grant (U.K.), award reference: EP/P020339, Royal Society Research Grant (U.K.), NSFC under Grant 61574138 and 61974131 and Major Scientific Research Project of Zhejiang Lab No. 2019MB0AD01, 20190057. (Corresponding authors: Henry Francis; Chao-Yuan Jin.)

Henry Francis, Si Chen, and Mark Hopkinson are with the Department of Electronic, and Electrical Engineering, University of Sheffield, Sheffield, S3 7HQ, United Kingdom (e-mail: hfrancis1@sheffield.ac.uk; schen62@sheffield.ac.uk; m.hopkinson@sheffield.ac.uk).

Xiao-Dong Zhang and Jia-Wang Yu are with the College of Information Science and Electronic Engineering, Zhejiang University, Hangzhou 310007, China, and also with the Zhejiang Lab., Hangzhou 311121, China (e-mail: zxd2019@zju.edu.cn; jw.yu@zju.edu.cn).

Kai-Jun Che is with the Department of Electronic Engineering, Xiamen University, Fujian 361005, China (e-mail: chekaijun@xmu.edu.cn).

Chao-Yuan Jin is with the Department of Electronic, and Electrical Engineering, University of Sheffield, Sheffield, S3 7HQ, United Kingdom, also with the College of Information Science and Electronic Engineering, Zhejiang University, Hangzhou 310007, China, and also with the Zhejiang Lab., Hangzhou 311121, China (e-mail: jincy@zju.edu.cn).

Color versions of one or more figures in this article are available at <https://doi.org/10.1109/JSTQE.2020.3041936>.

Digital Object Identifier 10.1109/JSTQE.2020.3041936

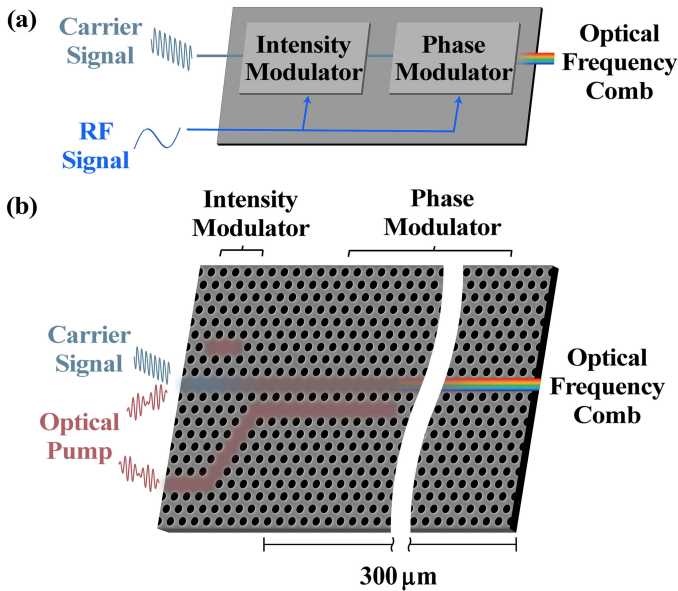


Fig. 1. (a) Schematic of OFC generation using cascaded electro-optic modulators (b) The proposed scheme superimposed, showing the implementation of (a) using PhC structures. RF-Radio Frequency.

The drawback of this system still resides in the overall size. The waveguide length is often on the order of centimetres to induce a sufficient modulation depth at low powers.

Other approaches to reduce device footprint have been proposed based on electro-absorption modulators. Nozaki *et al.* [16] demonstrated a low energy electro-absorption modulator based on a InGaAsP-embedded PhC waveguide. However this involved complex fabrication techniques to obtain a p-i-n junction across the micro-scale waveguide. Decreased size and complexity as well as chip-scale integration are a necessity for future photonic circuits and modulators based on EO interaction become increasingly hard to implement when scaling down. Conversely, all-optical modulators show great potential in micro- and nano-scale devices due to the enhanced light-matter interaction, this negates the need for complex and bulky electronic interconnects. In this way, OFC generation based on all-optical modulation shows strong potential for scaling down device size while maintaining the characteristics of modulation-based OFCs.

Optical defects in PhC lattices produce cavities and waveguides that have the ability to modulate the intensity and phase of an input carrier light, as shown in Fig. 1. The high Q/V ratio in PhC cavities leads to highly nonlinear optical processes which facilitate low power all-optical intensity modulation (IM). Switching energies of less than 1 femtojoule per bit [7] have been demonstrated for PhC cavity-based IM and a range of material platforms have been studied to tailor the operation wavelength and modulation bandwidth [17]–[19]. Embedded quantum dots (QDs) in a PhC waveguide enhance third order nonlinear susceptibility which causes cross phase modulation through saturable absorption of the QD layer [20]–[22]. A pulsed pump light can therefore modulate the phase of an input carrier light via a PhC waveguide. In this study, cavity-based all-optical modulation followed by waveguide-based phase modulation (PM) is analysed for the generation of OFCs.

The proposed photonic circuitry is outlined in Fig. 1(b), the optical modulation signal is split and enters the device via the two input waveguides. These two input waveguides are shown on the left of Fig. 1(b). A similar integration scheme can be found in Ref. [22]. The optical modulation signal in the upper arm generates intensity modulation of the carrier signal via the L3 cavity. The optical modulation signal in the lower arm interacts with the carrier signal in the $600 \mu\text{m}$ waveguide that follows the cavity-based IM, causing PM of the carrier signal. Schemes based on multiple PhC cavities or the coupling of multiple PhC waveguides is common and relies on confocal microscopy to direct and collect light to and from different parts of nano- and micro-scale devices. Different integration schemes are explored to realise OFCs with a tunable mode spacing and broad spectral range.

II. MODELLING CAVITY-BASED ALL-OPTICAL MODULATION

The device structure comprises of two layers of InAs QDs emitting around 1550 nm embedded in a 220 nm thick InP membrane. Holes are etched into the membrane in a triangular lattice in order to produce a photonic bandgap. A lattice constant of 480 nm and fill factor of 0.29 ensure a fundamental mode wavelength at 1551 nm when three holes are removed to produce an L3 cavity. The fundamental mode of an L3 cavity with these dimensions has been simulated using COMSOL and shown in Fig. 2(c). To create a waveguide through which light within the photonic bandgap can propagate, a line of holes are removed from the structure, as depicted in Fig. 2(a) and 2(b). Two schemes to implement IM using PhC cavities have been studied here, they are side coupled and direct coupled cavity-waveguide structures, as shown in Fig. 2(a) and 2(b), respectively.

All-optical modulators based on PhC structures is a well-established technique [7], [23], [24] in which various optical nonlinearities are utilised. In the device proposed here, the optical nonlinear medium is based on the saturable absorption of embedded quantum dots. A model based on temporal coupled mode theory (CMT) [17], [25] is used to numerically analyse the optical modulation characteristics of the two schemes shown in Fig. 2(a) and 2(b). The equations used in this paper are derived from common CMT techniques for the modelling of PhC all-optical switches [17], [18], [26], [27]. The simulations are carried out by solving Eqs. (1), (2), (5)–(7) numerically using a standard routine for solving ordinary differential equations. Eqs. (6) and (7) give output from the side and direct coupled cavity IM schemes. The output from the different IM schemes lead into the input of the PM, as outlined in Fig. 1. The physical parameters used are shown in Table I. The material system is made up of a InP membrane with InAs quantum dots embedded within the membrane.

Since optical nonlinear effects are the basis for realising a cavity resonance shift, it's necessary to analyse the nonlinear process in the target situation. In principle, any type of non-linearity can be utilised for shifting the cavity resonance, in this study, both carrier and intensity-based nonlinearities are considered. By exciting a PhC cavity with an increasing pump energy, the refractive index of the cavity material will decrease

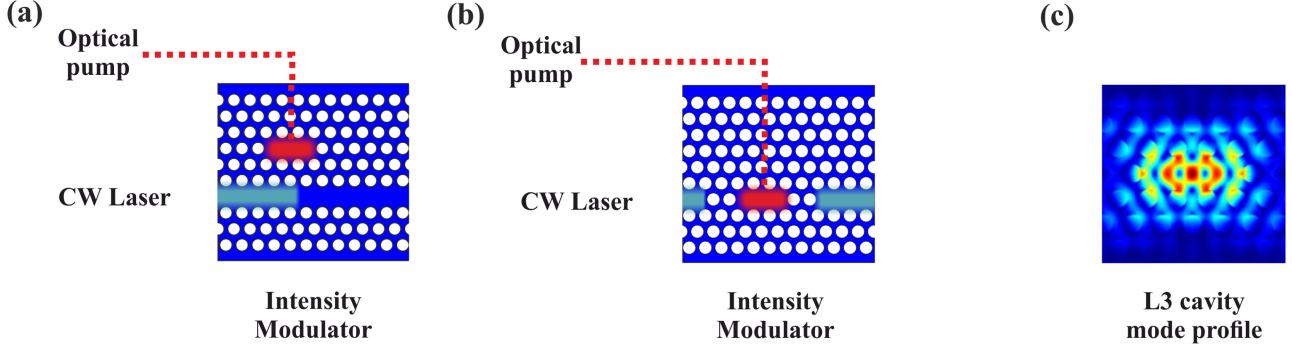


Fig. 2. (a) Side coupled cavity modulation scheme (b) Direct coupled cavity modulation scheme (c) Mode profile of L3 cavity.

TABLE I
PARAMETERS USED FOR CMT CALCULATIONS

Symbol	Parameter	Value
Q_{int}	Intrinsic Q factor	30000 [24]
Q_c	Coupling Q factor	9130 [24]
γ_{QD}	Decay rate of carriers in QDs	$1.25 \times 10^{10} \text{ s}^{-1}$ [30]
σ_{FCA}	FCA cross section	$4.5 \times 10^{21} \text{ m}^2$ [17]
β	TPA coefficient	$2.4 \times 10^{-10} \text{ m/W}$ [17]
V_{TPA}	TPA volume	$3.13(\lambda/n)^3$ [24]
n_2	Enhanced Kerr coefficient	$1.24 \times 10^{-15} \text{ m}^2/\text{w}$ [31]
n	Refractive index	3.17 [17]
V_{car}	Free carrier cavity volume	$4.62(\lambda/n)^3$ [24]
τ_{fc}	Free carrier lifetime	50ps [17]
α	Scattering loss of PhC waveguide	230 m^{-1} [32]
n_g	Group index	40 [20], [33]

due to free carrier dispersion [28] through carriers excited by two photon absorption (TPA), this term is calculated using Eq. (4). Bandfilling is another common phenomenon used in all-optical switching where the material absorption changes as the conduction bands are filled. However, this can only be utilised when the cavity resonance is close to the band edge of the bulk material. Therefore this effect can be neglected due to the use of an InP-based membrane structure. In addition to this, absorption of the QD layer within the membrane leads to an enhanced third order nonlinear susceptibility [5], [21], [29] which will change the refractive index of a material, as defined through the Kerr coefficient in Eq. (3). Cavity resonance shifts due to thermal effects occurs over a relatively long time [11]. The dynamic variables in the model are the field amplitude and the free carrier density inside the cavity.

The devices shown in Figs. 2(a) and 2(b) are driven by an input field from the left waveguide, the field amplitude in the waveguide is given by $s_{p,c}^{in}$, where p and c represent the pump and carrier light respectively. The amplitude of the cavity field is given in the form $a_{p,c}$. The energy of the field in the cavity is $|a_{p,c}(t)|^2$ and the power of the field in the waveguides is equal to $|s_{p,c}^{in}(t)|^2$. Using the slowly varying envelope approximation to define the field amplitude in the cavity gives the relation:

$$\frac{da_{p,c}(t)}{dt} = (-i(\omega_0 + \Delta\omega_{p,c}(t)) - \omega_{p,c}) - \gamma_{total}/2 a_{p,c}(t) + u s_{p,c}^{in}(t) \quad (1)$$

It is assumed that $a_p(t) \gg a_c(t)$, so only $a_p(t)$ will have an effect on the change in cavity resonance, denoted by $\Delta\omega_p$. In Eq. (1), ω_0 is the angular frequency of the cold cavity resonance, $\omega_{p,c}$ is the angular frequency of the input light, for either the pump or carrier light. The total energy decay rate in the cavity is represented by $\gamma_{total} = \gamma_{int} + 2\gamma_c + \gamma_{QD} + \gamma_{FCA} + \gamma_{TPA}$. The intrinsic loss rate γ_{int} is dependent on the vertical Q factor of the cavity, such that $\gamma_{int} = \omega_0/Q_{int}$. $\gamma_c = \omega_0/Q_c$ represents the coupling strength between the cavity and the waveguides. γ_{QD} represents QD absorption recovery time. γ_{TPA} and γ_{FCA} represent the losses due to optical absorption via TPA and free carrier absorption (FCA), respectively. The coupling coefficient is defined as $u^2 = 2\gamma_c$ [25]. The shift in cavity resonance is dependent on the energy inside the cavity and the density of generated free carriers, given by:

$$\Delta\omega_p(t) = -(K_{kerr}|a_p(t)|^2 - K_{fcd}N_c(t)) \quad (2)$$

K_{fcd} represents the contribution from free carrier dispersion in the InP membrane which blueshifts the resonance frequency [17]. K_{kerr} represents a simplified value for the third order nonlinear dynamical process [7], [24] which redshifts the cavity resonance. K_{kerr} and K_{fcd} are given by:

$$K_{kerr} = \frac{\omega_0 c n_2}{n_{eff}^2 V_{kerr}} \quad (3)$$

$$K_{fcd} = \frac{e^2}{2n^2 \omega_0 \varepsilon_0 m_0} \quad (4)$$

where e is the elementary electric charge, n is the refractive index of InP, ε_0 is the vacuum permittivity, m_0 is the effective mass of carriers and c is the speed of light in vacuum. n_2 is the cavity-enhanced nonlinear refractive index coefficient [21], [29], which is enhanced by the QDs in the membrane due to a single elect-hole pair generating transparency of the ground state transition. V_{Kerr} is the Kerr nonlinear volume used to characterise the average saturable absorption rate in the cavity. Due to the small modal volume in the PhC cavity and the saturable absorption of the QDs the optical nonlinear effect is greatly enhanced and therefore dominates the switching process [20], [24]. $N_c(t)$ gives the carrier generation term due to TPA in the

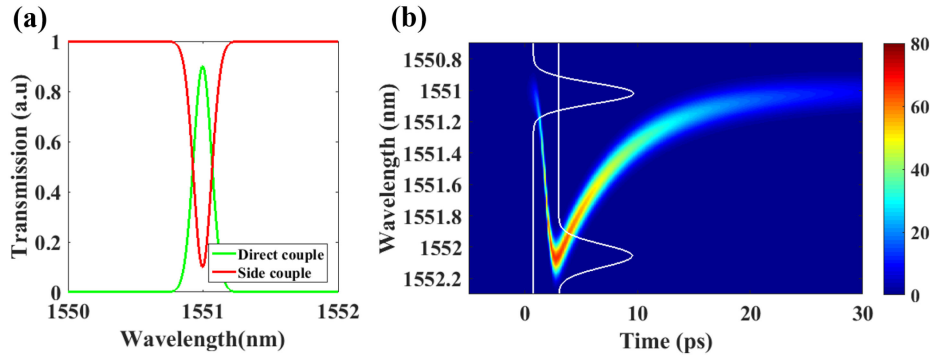


Fig. 3. (a) Frequency domain transmission characteristics for both the side and direct coupled cavity scheme. (b) A 3D plot, showing how the resonant cavity modes shifts when a pump light is incident on the device, the white lines represent the mode spectrum at 0 ps and 3 ps, respectively.

device [17], [18], this is given by:

$$N_c(t) = \frac{|a_p(t)|^2}{\tau_{TPA}} \frac{1}{2\hbar\omega_0} \frac{1}{V_{cav}} \tau_{fc} \quad (5)$$

where \hbar is Planck's constant, τ_{fc} is the free carrier lifetime and V_{cav} is the cavity volume for free carriers [24]. Fig. 3(a) shows the transmission characteristics for both the side and direct coupled scheme. In the direct coupled scheme, when the frequency of the propagating wave and the cavity resonance are equal, the light can transmit to the output waveguide. At all other frequencies, the light reflects at the waveguide-cavity interface. Conversely, for the side coupled scheme the interference between the energy in the cavity and the propagating wave through the waveguide causes a drop in the transmission at the cavity resonance. However, at all other frequencies, the wave can transmit through the device. To generate an all-optical switch, the cavity resonance can be perturbed via optically induced nonlinear interactions. Fig. 3(b) is a 3D map which shows the perturbation of the cavity resonance with the presence of a pump pulse. The white lines in Fig. 3(b) show the cavity mode spectrum. It gives an illuminating example that shows how a so-called cavity switch works when a very short pulse of 1.5 ps excites the nanophotonic cavity [7], [17]. The cavity mode goes from 1551 nm and increases to 1552 nm when the pump pulse is incident. When the direct coupled scheme is used, the carrier light wavelength is set to 1552 nm. The pump light will cause the cavity to come into resonance with the carrier light, hence generating transmission of the carrier light. For the side coupled scheme, the carrier light is set to the initial cold cavity resonance at 1551 nm, meaning that no light can transmit through the device. The pump light causes the cavity to come out of resonance with the carrier light, hence allowing transmission. As shown in Fig. 3(a), a resonance wavelength shift of 1 nm will cause a drastic change in the transmission characteristics, thus implementing all-optical intensity modulation. To induce this change within the cavity, a refractive index change of 0.002 is needed. Achieving this refractive index change using PhC cavities is common amongst the nanophotonics research community [5], [22].

In the side coupled scheme, shown in Fig. 2(a), the output of the device will be dependent on the energy inside the cavity,

the coupling factor and the energy from the input directly. This gives rise to:

$$s_c^{out}(t) = u \frac{a_c(t)}{2} + s_c^{in}(t) \quad (6)$$

s_c^{out} is the field amplitude in the output waveguide. Conversely, in the direct coupled scheme, shown in Fig. 2(b), the output energy will only depend on the energy coupled into the waveguide from the cavity. This gives rise to Eq. (7):

$$s_c^{out}(t) = u \frac{a_c(t)}{2} \quad (7)$$

By using a pump light with a sinusoidal waveform that has a repetition frequency of 10 GHz, it is possible to observe different output dynamics from each coupling scheme.

Fig. 4(a) shows one pulse of the sinusoidal waveform, given by the dashed line and the intensity modulated carrier light at the output of the side coupled cavity-based IM, given by the solid black line. The output from this side coupled scheme shows a broad, asymmetric pulse. This shape is due to the carrier light transmitting through the device as soon as its frequency is shifted from the cavity resonance. A sharp increase in the transmission is observed since the energy does not go through the cavity to reach the output. At its maximum, the power from the input light is being transferred to the output with only a small portion coupling into the cavity. The frequency response of the carrier light is given in Fig. 4(b). The broad pulse size dictates that the side bands produced through sinusoidal modulation are heavily suppressed. Their position relative to the carrier light frequency at 193.42 THz is a direct relation to the modulation frequency at 10 GHz.

The temporal response of the carrier light through a direct cavity modulator matches the pump light more closely than the side coupled modulation scheme. As the cavity resonance goes towards the carrier light frequency, more energy can transfer to the output waveguide, therefore matching the modulation light closely, as show in Fig. 4(c). The frequency response at the output of the direct coupling IM scheme is given by Fig. 4(d). Prominent side bands are present for the direct coupled scheme because the signal has a more sinusoidal profile with a slightly flat-topped peak. The observation of side bands produced from a

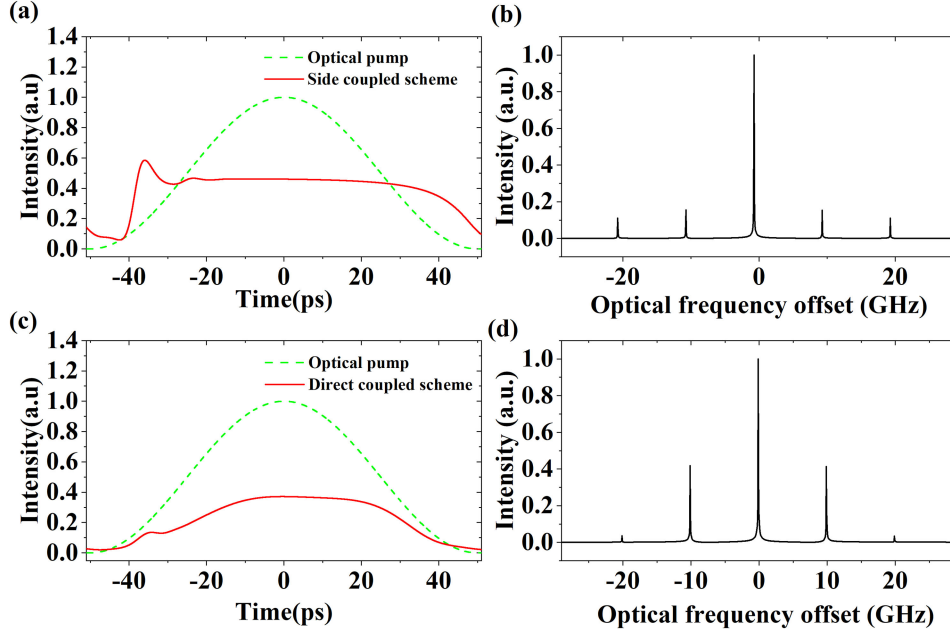


Fig. 4. (a)–(b) Side coupled cavity IM scheme. (a) The time domain response of the modulated carrier (solid black line) and the optical pump (green dashed line) light. (b) The frequency domain response of the intensity modulated carrier light. (c)–(d) Direct coupled cavity IM scheme. (c) The time domain response of the modulated carrier (solid red line) and the optical pump (green dashed line) light. (d) The frequency domain response of the intensity modulated carrier light.

PhC cavity-waveguide integration scheme at the telecommunications wavelength shows a promising step towards all-optical signal processing [34].

III. IMPLEMENTING PHASE MODULATION VIA PHC WAVEGUIDES

The output from the IMs, given in Eqs. (6) and (7), is fed into an all-optical phase modulator implemented via a PhC waveguide. In this scheme, a pump light is used to induce saturable absorption of QDs in the waveguide, which leads to a refractive index change in the waveguide material via Kramers-Kronig relation [31]. The carrier light experiences a corresponding refractive index change, resulting in a phase shift of the carrier light. This phase shift is therefore proportional to the intensity profile of the pump light [20], [31]. In this study, a single optical pump light is used for both the intensity and phase modulator, this ensures coherence between the two modulators. The induced phase shift is calculated using standard equations for PM:

$$E^{out}(t) = |s_c^{out}(t)|^2 \exp(i\Delta\theta - \alpha L_{wg}) \quad (8)$$

$s_c^{out}(t)$ is the output from either the side or direct coupled scheme. α is the scattering loss within the waveguide. The propagating signal will deplete due to both scattering losses and TPA induced attenuation. TPA is a nonlinear effect and is included in the nonlinear refractive index coefficient. $\Delta\theta$ is the phase modulation index (PMI) in a PhC-waveguide PM [35], given by:

$$\Delta\theta(t) = -k_0 L_{wg} \frac{n_g}{n_0} n_2 \frac{|s_p^{in}(t)|^2}{A} \quad (9)$$

where k_0 is the wavenumber in vacuum, L_{wg} is the waveguide length, n_g is the group index and A is the cross section of the waveguide mode. The nonlinear refractive index coefficient in the waveguide, n_2 , is derived from the literature, where similar schemes have been realised [20], [31], [33]. This is estimated to be $1.24 \times 10^{-15} \text{ m}^2/\text{W}$. The PMI is therefore dependant on two key parameters, the length of the waveguide and the power of the pump light. The sinusoidal shape of the pump light will induce a quadratic phase shift for the duration of the carrier pulse. With a quadratic phase shift of the carrier pulse, the signal can be accurately mirrored from the time domain into the frequency domain [36]. Therefore, the PhC waveguide-based PM will dramatically increase the number of sidebands in the carrier signals frequency spectrum, hence generating an OFC. The output response in the frequency domain from the PM is calculated via the Fourier transform and plotted in Fig. 5. This phenomenon has previously been reported for EO modulators, in this case all-optical devices with a micron-scale footprint have been used to realise modulation-based OFC generation. Using a waveguide length of $600 \mu\text{m}$, an OFC can be produced using both the side and direct cavity-waveguide scheme as well as without a preceding IM as shown by Fig. 5. Although the use of a waveguide-based PM increases the overall device geometry, a waveguide length within the hundreds of microns shows a significant reduction in size when compared to EO waveguide-based PMs. To further scale down the size of PM devices, PhC cavities can be considered which will generate a scalable phase change by increasing the Q factors within a small cavity of micron meter size [37].

Without a preceding IM, an OFC is produced, this is shown in Fig. 5(a). The benefit of a cascading IM-PM scheme can be seen

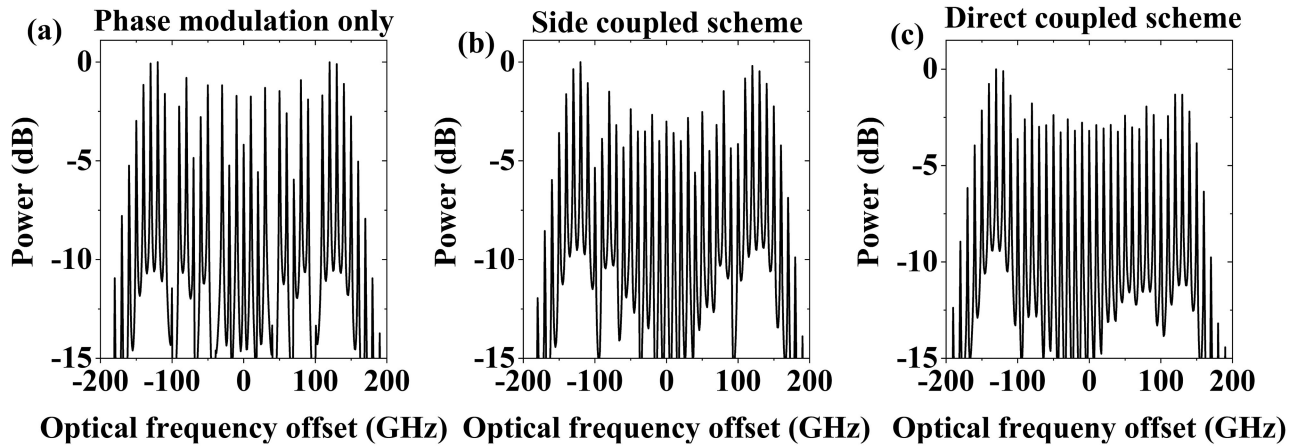


Fig. 5. The generated OFCs at the output of the device (a) shows the output without a PhC IM used, (b) shows the OFC using the side coupled cavity scheme and (c) shows the OFC from the direct coupled cavity scheme.

from the comparison of Fig. 5(a) to Fig. 5(b) and 5(c). The resulting comb from the PM only scheme shows a non-flat spectrum, where the maximum comb line difference has been calculated to provide a figure of merit concerning the comb flatness. In the case of PM without a preceding IM, the difference is 13.3 dB. This is improved to 5.6 dB for the direct coupled scheme and down to 3.6 dB for the side coupled scheme. Fig. 4(a) shows the output from the IM in the time domain when the side coupled scheme is used. In this IM scheme, output pulse is slightly broader than the sinusoidal pump pulse used for modulation, as shown in Fig. 4(a). This means that at the beginning and end of each carrier pulse the induced phase shift will be very small, resulting in points where the instantaneous frequency function dwells and a drop in comb line power is observed. This can be seen in the resulting OFC, given in Fig. 5(b), where the comb line power drops at around -50 GHz and 50 GHz.

Conversely, the direct coupled cavity waveguide scheme follows the shape of the sinusoidal input more closely, as shown in Fig. 4(c). The field amplitude in the output waveguide reaches its high output value when the pump light is close to the top of the sinusoidal curve. This results in a pseudo-parabolic phase shift being incident on the carrier pulse for the time that it is high. This gives rise to more accurate mirroring of the signal and therefore a flatter comb, as shown in Fig. 5(c). There are exaggerated comb lines around the OFC minima and maxima at -100 GHz and 100 GHz respectively. The slightly asymmetric shape of the output carrier light from the IM and the phase mismatch between the peak of the sinusoidal wave and the peak of the output wave, as depicted in Fig. 4(c), cause these exaggerated comb lines.

An important variable when analysing the functionality of an OFC generator is the amount of input power needed to generate the resulting comb. In all calculations, the pump power is split between the IM and PM with a total pump power of 50 mW. The very high light confinement obtainable in the L3 cavity dictates that the amount of power needed from the pump light to induce sufficient switching of the carrier light is less than the waveguide-based PM. It is found that a pump light power of 10 mW causes sufficient intensity modulation. However a

pump light power of 40 mW is needed to induce sufficient PM of the carrier light. This higher power needed for the PM when compared to the IM is due to scattering of light in the waveguide and its larger size. These input powers are assumed throughout the paper with exception of section IV, where the pump power is scaled equally for both the IM and PM.

IV. SYSTEM OPTIMISATION

In the previous section, two cavity-waveguide intensity modulator configurations have been compared. It has been found that a direct cavity-waveguide configuration leads to a flatter OFC. In this section the characteristics of the pump light used to modulate the carrier light are analysed for the direct coupled scheme. Manipulation of the pump light modulation speed and power lead to a change in the resulting OFC characteristics. Through this analysis and manipulation, it is possible to optimise the system to increase spectral bandwidth of the OFC and increase comb line power homogeneity. It is therefore possible to tune the output of the device and increase the application versatility.

Using PhC-based OFC generation, the spacing between the comb lines can be tuned by the modulation frequency, this leads to a number of varied applications. For example, tightly confined frequency components are needed for optical frequency synthesis of microwave signals [38], this can be achieved by decreasing the modulation frequency. However, for wavelength division multiplexing a broader comb can prove beneficial as it spans over a larger frequency band [39]. By increasing the modulation frequency, the spacing between the comb lines is increased, hence broadening the comb. The maximum modulation bandwidth of the PhC-based IM is a product of the cavity resonance switching time. The switching time, governed by the device properties, will limit the modulation speed. To find the maximum modulation speed, a pump pulse with a pulse duration of 1.5 ps is incident on the cavity. Fig. 3(b) shows the dynamical change of the cavity resonance using a 1.5 ps pump pulse. The cavity switching time calculated here is less than 10 ps. Therefore, the maximum spacing between comb lines is limited

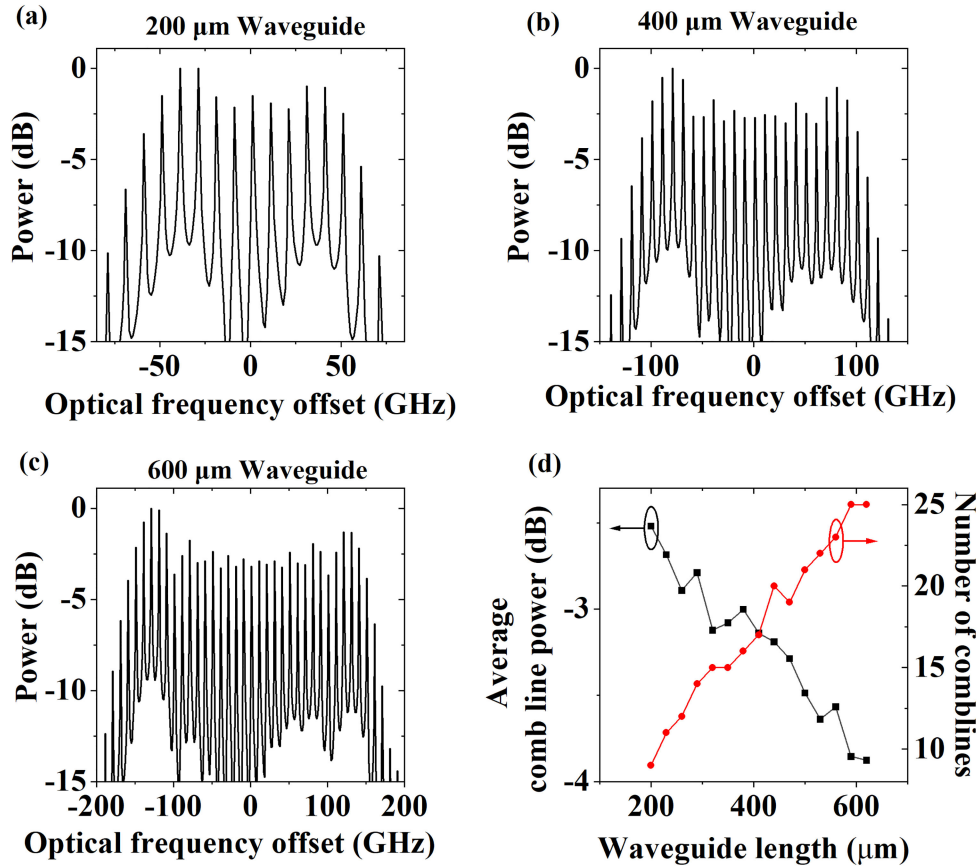


Fig. 6. Effect on OFC generation by increasing the waveguide length (a) 200 μm waveguide, (b) 400 μm waveguide (c) 600 μm waveguide (d) shows the flatness and number of generated comb lines against waveguide length.

to 100 GHz. However, increasing the modulation speed above 100 GHz causes significant reduction in the modulation depth attainable from the PhC IM. The repetition rate can also be tuned to produce very close comb lines in the OFC spectrum.

It is possible to increase the number of comb lines in the OFC at the output of the devices through manipulation of the waveguide length. As shown in Eq. (9), the PMI depends on the power of the pump light and the length of the PhC waveguide. A longer waveguide will enhance the PMI and therefore increase the spectral width of the OFC. In this study, the modulation speed is set to 10 GHz, which leads to an spacing of 10 GHz between the comb lines, the length of the waveguide is then increased from 200 μm up to 600 μm . Fig. 6(a) shows a waveguide length of 200 μm , the resulting OFC spans over 100 GHz, Fig. 6(b-c) show waveguide lengths of 400 μm and 600 μm , respectively. Although the number of comb lines and therefore spectral width of the OFC is increasing it comes at the cost of comb line intensity homogeneity. By calculating the relative power for each of the generated comb lines, an average comb line power can be found which correlates to the overall flatness of the comb. As the waveguide length increases, the average comb line power steadily decreases, as shown in Fig. 6(d). This is because the area over which the quadratic phase shift is induced on the pulses is increasing. As the area increases, the pump light that is incident on the carrier pulse causes dwelling of the frequency function on

the outer edges of the OFC, inducing greater comb line power disparity.

The number of comb lines and therefore the spectral broadness of an OFC can also be optimised by the power of the pump light used. An increased pump light power will cause a greater resonance shift in the cavity as well as increasing the PMI of the waveguide-based PM. An increase in the power of the pump light will lead to a larger phase shift of the carrier light, thus increasing the spectral broadness of the resulting OFC. However, by increasing the power of the pump light going to the IM, a larger cavity resonance change takes place. This has a detrimental effect on the shape of the carrier light at the IM output because the cavity resonance shifts away from the carrier light wavelength at peak pump light power. As shown in Fig. 7(a), when increasing the pump light power the output from the IM using the original carrier light wavelength (red curve) has a large dip when the pump light is at its maximum, at time 0. This is due to the large wavelength mismatch between the carrier light and cavity resonance at this point. When this signal undergoes quadratic phase modulation via the PhC waveguide, this shape is mirrored in the frequency domain where a large dip is present in the OFC output spectrum, shown in Fig. 7(b). Although the intensity of the comb lines in Fig. 7(b) is not flat, the OFC spectral range has been improved to span over 600 GHz, this is due to the increased power in the PhC waveguide.

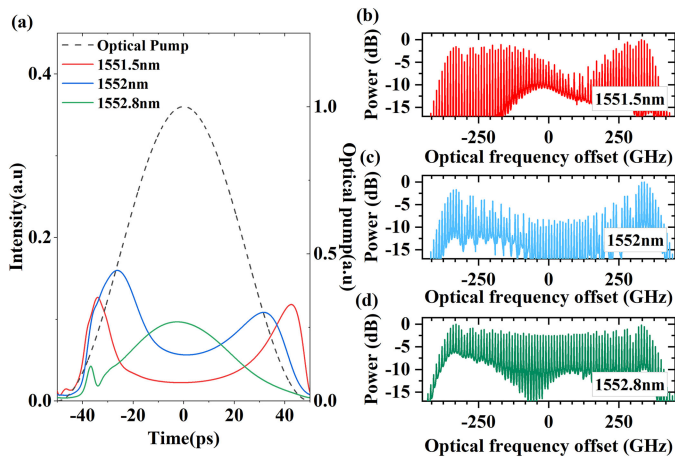


Fig. 7. (a) Increased optical pump light (dashed line) with output of IM with no wavelength change (red), 1 nm wavelength change (blue) and 1.5 nm wavelength change (green). (b) The frequency response after PM for 0 nm shift, (c) 0.5 nm shift, (d) 1.3 nm shift.

To generate a flatter comb, a flatter topped pulse is needed from the IM. To obtain this, the carrier light frequency can be tuned so that it matches the cavity resonance when the pump light is at its peak value. The blue curve in Fig. 7(a) shows the output of the IM using a 0.5 nm red shifted carrier light. A flatter OFC is observed in the frequency domain at the output of the device. To increase the homogeneity of the OFC the carrier light can be shifted further, the green curve shows a 1.3 nm shifted carrier light. By shifting the carrier light by 1.3 nm, a flat-topped pulse is produced in the time domain. The corresponding time to frequency converted spectrum, Fig. 7(b-d), shows that by increasing the pump light power and shifting the carrier frequency the spectrum is increased to span over 600 GHz and its homogeneity improved dramatically.

During experimental implementation of the proposed scheme there will be disparity between the optimised parameters given here and the fabricated device. During manufacturing, fluctuation in etching parameters could lead to a difference in surface passivation of the PhC sidewalls. This will cause both angled and rough sidewalls which will degrade the light confinement properties of the PhC. For the cavity-based IM, this will mean a lower obtainable Q and for the waveguide-based PM, this will decrease the obtainable PMI. In both instances, this will lead to a higher optical modulation signal power needed to obtain the results given in Fig. 7(b-d). During fabrication, trade-offs exist between etch depth, sidewall angle, etch temperature, etch speed and many more. Therefore, results using an angled sidewall have not been simulated here because the specific angle is highly dependent on the fabrication parameters.

In experimental realisation, the bandwidth of the comb may reduce slightly from the simulated results due to input and output coupling from the device. This may also affect the power efficiency of the device, coupling light into PhC waveguides is notoriously difficult due to the very small dimensions, leading to low efficiencies. Having said this, PhC devices are a mature research field where fabrication and characterisation are common

place to many institutes; as such, successful implementation of this technique experimentally is feasible and expected.

V. CONCLUSION

To summarise, a novel approach to generating OFCs is proposed using PhC devices. A theoretical study, developed using temporal CMT has provided validation to the realisation of OFCs on this scale. The model consists of all-optical PhC modulators that are driven by optical waveforms at a repetition frequency in the RF range. Initially, a single PhC cavity is used to modulate a continuous wave at laser 1550 nm. Multiple peaks are observed around 1550 nm, with a mode spacing matching the pump light modulation frequency. The mode spacing is directly proportional to the modulating frequency, thus providing a tunable on-chip microwave photonic source which can extend up to the modulation bandwidth of the PhC device. A PhC waveguide-based phase modulator is then introduced to increase the number of generated sidebands. Different integration schemes have been analysed to extend the bandwidth of the produced OFC. The results indicate that a direct coupled cavity modulator will achieve a flatter comb and hence be preferred for integrated OFCs. Further analysis and optimisation of the pump light characteristics and device parameters produce a very flat OFC that spans over 600 GHz. The resulting structures have excellent potential for applications in photonic integrated circuits and optical signal processing.

ACKNOWLEDGMENT

The authors would like to thank Prof. Osamu Wada for his insightful comments and input throughout.

REFERENCES

- [1] D. Marpaung, J. Yao, and J. Capmany, "Integrated microwave photonics," *Nat. Photon.*, vol. 13, Feb. 2019.
- [2] C. Haffner *et al.*, "All-plasmonic Mach-Zehnder modulator enabling optical high-speed communication at the microscale," *Nat. Photon.*, vol. 9, no. 8, pp. 525–528, 2015.
- [3] D. Marpaung *et al.*, "Low-power, chip-based stimulated Brillouin scattering microwave photonic filter with ultrahigh selectivity," *Optica*, vol. 2, no. 2, pp. 76–83, 2015.
- [4] V. Brasch *et al.*, "Photonic chip based optical frequency comb using soliton Cherenkov radiation," *Science*, vol. 351, no. 6271, 2016.
- [5] C.-Y. Jin and O. Wada, "Photonic switching devices based on semiconductor nano-structures," *J. Phys. D: Appl. Phys.*, vol. 47, no. 13, 2014.
- [6] H. Francis, S. Chen, K.-J. Che, M. Hopkinson, and C.-Y. Jin, "Photonic crystal cavity-based intensity modulation for integrated optical frequency comb generation," *Crystals*, vol. 493, pp. 1–10, 2019.
- [7] K. Nozaki *et al.*, "Sub-femtojoule all-optical switching using a photonic-crystal nanocavity," *Nat. Photon.*, vol. 4, no. 7, pp. 477–483, 2010.
- [8] K. Nozaki *et al.*, "Femtofarad optoelectronic integration demonstrating energy-saving signal conversion and nonlinear functions," *Nat. Photon.*, vol. 13, no. 7, 2019.
- [9] Y. Ota, R. Katsumi, K. Watanabe, S. Iwamoto, and Y. Arakawa, "Topological photonic crystal nanocavity laser," *Commun. Phys.*, vol. 86, pp. 4–6, 2018.
- [10] A. L. Gaeta, M. Lipson, and T. J. Kippenberg, "Photonic-chip-based frequency combs," *Nat. Photon.*, vol. 13, no. 3, 2019.
- [11] P. Marin-Palomo *et al.*, "Microresonator-based solitons for massively parallel coherent optical communications," *Nat.*, vol. 546, pp. 274–279, 2017.
- [12] V. Torres-Company and A. M. Weiner, "Optical frequency comb technology for ultra-broadband radio-frequency photonics," *Laser Photon. Rev.*, vol. 8, no. 3, pp. 368–393, 2014.

- [13] A. Delamde, M. Krstic, C. Browning, J. Crnjanski, D. Gvozdic, and B. Laim, "Power efficient optical frequency comb generation using laser gain switching and dual-drive Mach-Zehnder modulator," *Opt. Express*, vol. 27, no. 17, pp. 24135–24146, 2019.
- [14] T. Ren *et al.*, "An integrated low-voltage broadband lithium niobate phase modulator," *Photon. Technol. Lett.*, vol. 31, no. 11, pp. 889–892, 2019.
- [15] Y. Qi and Y. Li, "Integrated lithium niobate photonics," *Nanophotonics*, vol. 9, no. 6, pp. 1287–1320, 2020.
- [16] K. Nozaki *et al.*, "Ultralow-energy electro-absorption modulator consisting of InGaAsP-embedded photonic-crystal waveguide," *APL Photon.*, vol. 2, no. 5, pp. 56105–56110, 2017.
- [17] Y. Yu *et al.*, "Switching characteristics of an InP photonic crystal nanocavity: Experiment and theory," *Opt. Express*, vol. 21, no. 25, pp. 31047–31061, 2013.
- [18] T. Uesugi, B.-S. Song, T. Asano, and S. Noda, "Investigation of optical nonlinearities in an ultra-high-Q Si nanocavity in a two-dimensional photonic crystal slab," *Opt. Express*, vol. 14, no. 1, pp. 377–386, 2006.
- [19] M. Notomi, A. Shinya, S. Mitsugi, G. Kira, E. Kuramochi, and T. Tanabe, "Optical bistable switching action of Si high-Q photonic-crystal nanocavities," *Opt. Express*, vol. 13, no. 7, pp. 2678–2685, 2005.
- [20] R. Prasanth *et al.*, "All-optical switching due to state filling in quantum dots," *App. Phys. Lett.*, vol. 84, no. 20, pp. 4059–4061, 2004.
- [21] H. Nakamura, S. Nishikawa, S. Kohmoto, K. Kanamoto, and K. Asakawa, "Optical nonlinear properties of InAs quantum dots by means of transient absorption measurements," *J. Appl. Phys.*, vol. 94, no. 2, pp. 1184–1189, 2003.
- [22] H. Nakamura *et al.*, "Ultra-fast photonic crystal/quantum dot all-optical switch for future photonic networks," *Opt. Express*, vol. 12, no. 26, pp. 6606–6614, 2004.
- [23] C. Y. Jin *et al.*, "Ultrafast non-local control of spontaneous emission," *Nat. Nanotechnol.*, vol. 9, no. 11, pp. 886–890, 2014.
- [24] A. De Rossi, M. Lauritano, S. Combrié, Q. V. Tran, and C. Husko, "Interplay of plasma-induced and fast thermal nonlinearities in a GaAs-based photonic crystal nanocavity," *Phys. Rev. A*, vol. 79, no. 4, pp. 1–9, 2009.
- [25] J. D. Joannopoulos, S. Johnson, J. N. J. Winn, and R. R. D. Meade, *Photonic Cryst. Molding Flow Light*. Princeton, NJ, USA: Princeton Univ. Press, 2nd ed., 2008.
- [26] I. Fushman, E. Waks, D. Englund, N. Stoltz, P. Petroff, and J. Vučković, "Ultrafast nonlinear optical tuning of photonic crystal cavities," *Appl. Phys. Lett.*, vol. 90, no. 9, pp. 2005–2008, 2007.
- [27] Y. Yu, E. Palushani, M. Heuck, D. Vukovic, and C. Peucheret, "Nonlinear switching dynamics in a photonic-crystal nanocavity," *Appl. Phys. Lett.*, vol. 071112, no. 2014, pp. 1–13, 2015.
- [28] B. R. Bennett, R. A. Soref, and J. A. Del Alamo, "Carrier-induced change in refractive index of InP, GaAs, and InGaAsP," *IEEE J. Quantum Electron.*, vol. 26, no. 1, pp. 113–122, Jan. 1990.
- [29] T. Kitada, T. Kanbara, K. Morita, and T. Isu, "A GaAs/AlAs multilayer cavity with self-assembled InAs quantum dots embedded in strain-relaxed barriers for ultrafast all-optical switching applications," *Appl. Phys. Express*, vol. 1, no. 9, 2008.
- [30] C. Y. Jin, O. Kojima, T. Kita, O. Wada, M. Hopkinson, and K. Akahane, "Vertical-geometry all-optical switches based on InAs/GaAs quantum dots in a cavity," *Appl. Phys. Lett.*, vol. 95, no. 2, pp. 2–5, 2009.
- [31] H. Nakamura, K. Kanamoto, Y. Nakamura, S. Ohkouchi, H. Ishikawa, and K. Asakawa, "Nonlinear optical phase shift in InAs quantum dots measured by a unique two-color pump/probe ellipsometric polarization analysis," *J. Appl. Phys.*, vol. 96, no. 3, pp. 1425–1434, 2004.
- [32] H. Oda, K. Inoue, Y. Tanaka, N. Ikeda, Y. Sugimoto, and K. A. Hiroshi Ishikawa, "Self-phase modulation in photonic-crystal slab line-defect waveguides," *Appl. Phys. Lett.*, vol. 90, no. 23, pp. 2005–2008, 2007.
- [33] R. Notzel and J. Haverkort, "InAs/InP self-assembled quantum dots: Wavelength tuning and optical nonlinearities," *Adv. Funct. Mater.*, vol. 10, 2006.
- [34] H. Francis *et al.*, "Generation of optical frequency combs using a photonic crystal cavity," *IET Optoelectronics*, vol. 13, no. 1, pp. 1–4, 2018.
- [35] K. Inoue, H. Oda, N. Ikeda, and K. Asakawa, "Enhanced third-order nonlinear effects in slow-light photonic-crystal slab waveguides of line-defect," *Opt. Express*, vol. 17, no. 9, pp. 7206–7216, 2009.
- [36] V. Torres-Company, J. Lancis, and P. Andres, "Lossless equalization of frequency combs," *Opt. Lett.*, vol. 33, no. 16, pp. 1822–1824, 2008.
- [37] C. Y. Jin, O. Kojima, T. Kita, O. Wada, and M. Hopkinson, "Observation of phase shifts in a vertical cavity quantum dot switch," *Appl. Phys. Lett.*, vol. 98, no. 23, pp. 2009–2012, 2011.
- [38] D. T. Spencer *et al.*, "An optical-frequency synthesizer using integrated photonics," *Nature*, vol. 557, no. 7703, pp. 81–85, 2018.
- [39] T. Healy, F. C. G. Gunning, A. D. Ellis, and J. D. Bull, "Multi-wavelength source using low drive-voltage amplitude modulators for optical communications," *Opt. Express*, vol. 15, no. 6, pp. 2981–2986, 2007.

Henry Francis received the master's degree (M.Eng) from Bangor University, Bangor, U.K., in 2015. He is currently the Ph.D. Candidate with the University of Sheffield. His research interests include microwave photonics, photonic integrated circuits and optical signal processing.

Xiao-Dong Zhang received the B.Sc. degree in microelectronics science and engineering from Xidian University, Xi'an, China, in 2019. He is currently studying for a master's degree with Zhejiang University.

Si Chen was born in Henan, China, in 1992. He received the B.S. degree from the Huazhong University of Science and Technology, Wuhan, China, in 2013 and the M.S. degree in semiconductors in 2015 from the University of Sheffield, Sheffield, U.K., where he is currently working toward the Ph.D. degree. His research interests include semiconductor-based ultrafast optical switches.

Jia-Wang Yu received the B.S. degree from the Wuhan University of Technology, Wuhan, China, in 2020. He is currently working toward the Ph.D. degree with Zhejiang University. His research interests include microwave photonics and quantum photonic chips.

Kai-Jun Che (Member, IEEE) was born in Linchuan, Jiangxi, China, in 1985. He received the Ph.D. degree in physical electronics from the Institute of Semiconductor, Chinese Academy of Science in 2010. He is currently an Associate Professor with the Department of Electronics Engineering, Xiamen University, Xiamen, Fujian, China. His research interests include semiconductor microlasers, plasmonic microdevices, optical nonlinearities, and optical devices applications.

Mark Hopkinson born in Nottingham, U.K. He received the B.Sc. degree from the University of Birmingham in 1985 and the Ph.D. degree from the University of Sheffield in 1990, both in physics. After appointments as Research Associate and Senior Researcher, he was appointed to a Chair of Electronic Engineering with the University of Sheffield in 2006. His research work concerns the growth of semiconductor nanostructures by Molecular Beam Epitaxy and their exploitation in advanced devices.

Chao-Yuan Jin received the Ph.D. degree from the University of Sheffield, Sheffield, U.K., in 2008. From 2008 to 2010, he was awarded a JSPS Postdoctoral Fellowship and worked on quantum dot switches with Kobe University, Japan. In 2010, he joined Eindhoven University of Technology, the Netherlands, as a Postdoctoral Researcher, working on ultrafast control of cavity quantum electrodynamics based on single quantum dots in photonic crystal cavities. From 2013 to 2015, he worked with a Dutch company EFFECT Photonics B.V. In his role as a Senior Photonics Scientist, he developed high-speed optical transceivers for short-reach optical communications based on generic photonic integration technologies. Then he was awarded the Vice-Chancellor's Fellowship and developed independent research programs on ultrafast photonic devices in the Department of Electronic and Electrical Engineering, University of Sheffield, U.K. He is currently working with Zhejiang University, China as a Professor. His research activities have focused on nanophotonic devices for optical signal and quantum information processing, including optical switches, lasers, single-photon sources, and nanophotonic integrated circuits.